



HAL
open science

Environmental changes in southeastern Europe over the last 450 ka: Magnetic and pedologic study of a loess-paleosol profile from Kaolinovo (Bulgaria)

D. Jordanova, Quentin Simon, S. Balescu, N. Jordanova, D. Ishlyamski, B. Georgieva, D.L. Bourles, A. Duvivier, Sophie S. Cornu

► To cite this version:

D. Jordanova, Quentin Simon, S. Balescu, N. Jordanova, D. Ishlyamski, et al.. Environmental changes in southeastern Europe over the last 450 ka: Magnetic and pedologic study of a loess-paleosol profile from Kaolinovo (Bulgaria). *Quaternary Science Reviews*, 2022, 292, 10.1016/j.quascirev.2022.107671 . insu-03824750

HAL Id: insu-03824750

<https://insu.hal.science/insu-03824750>

Submitted on 21 Oct 2022

HAL is a multi-disciplinary open access archive for the deposit and dissemination of scientific research documents, whether they are published or not. The documents may come from teaching and research institutions in France or abroad, or from public or private research centers.

L'archive ouverte pluridisciplinaire **HAL**, est destinée au dépôt et à la diffusion de documents scientifiques de niveau recherche, publiés ou non, émanant des établissements d'enseignement et de recherche français ou étrangers, des laboratoires publics ou privés.



Distributed under a Creative Commons Attribution - NonCommercial - NoDerivatives 4.0 International License



Environmental changes in southeastern Europe over the last 450 ka: Magnetic and pedologic study of a loess-paleosol profile from Kaolinovo (Bulgaria)

D. Jordanova^{a,*}, Q. Simon^{b,c}, S. Balescu^d, N. Jordanova^a, D. Ishlyamski^a, B. Georgieva^a, D.L. Bourlès^b, A. Duvivier^b, S. Cornu^b

^a National Institute of Geophysics, Geodesy and Geography, Bulgarian Academy of Sciences, Acad. G. Bonchev Bl.3, 1113, Sofia, Bulgaria

^b Aix Marseille Univ, CNRS, IRD, INRAE, Coll France, CEREGE UM 34, Aix en Provence, 13545, France

^c Walloon High Strategic Council, Place Joséphine-Charlotte 2, 5100, Namur, Belgium

^d Université de Lille, Laboratoire Halma (UMR 8164, CNRS), Bâtiment de Géographie, 59655, Villeneuve D'Ascq Cedex, France

ARTICLE INFO

Article history:

Received 30 April 2022

Received in revised form

3 July 2022

Accepted 18 July 2022

Available online 8 August 2022

Handling Editor: Mira Matthews

In Memory of Didier Bourlès, Prof. at CEREGE, who made this work feasible.

Keywords:

Pedogenic iron oxides

Quaternary

Environmental magnetism

Paleoclimate

Pedology

ABSTRACT

Magnetic properties are sensitive paleoenvironmental proxies frequently used in studies of loess paleosol profiles. Understanding precisely the magnetic recording of soil responses to environmental and climatic changes needs combining pedologic data and geophysical proxies. Here we present a new high-resolution study of a 450 ka old loess-paleosol profile from low Danube loess area at Kaolinovo (NE Bulgaria). The profile consists of Holocene soil S_0 on top, three paleosol units (S_1 , S_2 , S_3 – S_4) and the intercalated loess horizons L_1 to L_4 . Mineral magnetic and rock magnetic data together with pedological parameters (particle size distribution, total, crystalline and amorphous iron, soil organic carbon, total nitrogen, cation exchange capacity, carbonate content) show systematic variations in response to environmental changes. Principal component analyses carried out separately on magnetic mineralogy, rock magnetic and pedological variables reveal the complex response of loess – paleosol sediments to changes in source material and climate. The observed sharp shift in coercivity of mineral magnetic carriers at depth of the third loess L_3 marks the change from low-coercivity mineral assemblages in older units to higher coercivity in the last three loess paleosol couplets (L_1 – S_0 , L_2 – S_1 , L_3 – S_2). This boundary is related to both dust source change and increased climate aridity. The observed spikes in concentration-dependent magnetic parameters in the lowermost part of the profile and particular magnetic and pedologic signature of the oldest deposits (S_3 – S_4 pedocomplex) suggest that it may result from tephra additions in the studied loess-paleosol sequence, tentatively correlated to cryptotephra layers in other terrestrial archives in the region like Tenaghi Philippon and lake Ohrid sedimentary sequences. This work demonstrated that using PCA tool for studying the significance and objective inter-relationships of multiple mineralogical, mineral magnetic and pedological characteristics along depth of loess – paleosol profiles is an exemplary approach for revealing the underlying sedimentary and environmental processes.

© 2022 The Author(s). Published by Elsevier Ltd. This is an open access article under the CC BY-NC-ND license (<http://creativecommons.org/licenses/by-nc-nd/4.0/>).

1. Introduction

Loess paleosol sequences are widespread Quaternary deposits at mid-latitudes. They have primary aeolian origin and have been formed as a result of glacial/interglacial climate oscillations (Pye, 1995; Muhs, 2013; Maher, 2016). Soils within these sedimentary

sequences developed over periods of increased weathering and climate amelioration at stable surface conditions during time windows of several tens of thousands of years (Past Interglacials Working Group of PAGES, 2016). Subsequent soil burial under increasing sedimentation of new aeolian dust material during glacial inception detached the soil from the zone of active near-surface geochemical and microbiological processes (Sheldon and Tabor, 2009; Retallack, 2019). Thus, paleosols formed and preserved information on past environments. The low Danube loess

* Corresponding author.

E-mail address: diana.jordanova77@abv.bg (D. Jordanova).

area is part of the European loess belt, linking Eastern and Western Eurasian loess deposits and already allowed documenting paleo-environmental changes down to 800 ka (Balescu et al., 2003; Radan, 2012; Jordanova et al., 2008).

Detailed multidisciplinary studies on loessic paleosols as environmental archives are still rare (Jia et al., 2020). Experimental rock magnetic methods have been applied to identify the magnetic carriers of paleoclimate signal and characterize soils that form under typical interglacial climatic regimes. These approaches provide useful diagnostic information to constrain models of soil development and understand future soils formation under global climatic change. Even though magnetic measurements detect predominantly the strongly magnetic iron oxides in soils, which constitute merely up to 3 wt% of the total Fe content (Cornell and Schwertmann, 2003), their characteristics and concentration variations along loess-paleosol sequences permit to track changes in local environmental conditions (Maher, 2011).

In our study we show that joined geophysical magnetic and pedological (paleo)sol studies give valuable input for revealing the formation conditions and role of strongly magnetic iron oxides (magnetite, maghemite) in development of specific pedo-features. This approach is developed to identify the interactions between sedimentological processes of aeolian dust deposition, climate change and soil formation. The objective is to test if the utilization of the complex multi-parameter approach in magnetic and geochemical characterization of the studied loess-paleosol sequence allows to explore the driving mechanisms behind the environmental correlations and reconstructions, utilizing single property such as low field magnetic susceptibility.

Moreover, we demonstrate that the underlying reason for the systematically weaker magnetic enhancement of older paleosols S_3 and S_4 arises from the combined effects of changes in the grain size of the parent loess material, and strong change in the magnetic coercivity and concentration of antiferromagnetic hematite fraction.

2. Study area

Lower Danube area is surrounded by the Carpathians and Balkans mountain chains to the north – northwest and south, and by the Black Sea to the East (Fig. 1a). This topographic setting controls the distinct paleoecological and geomorphic conditions under which loess-paleosol sequences formed since 800 ka. Jipa (2014) outlined the evolution of low Danube loess deposits, emphasizing on the gradation of textural classes related to the distance from the Danube river and the role of Carpathian/Balkan range as a source of detrital inputs. The Kaolinovo site is located at the southernmost part of the continuous loess cover in NE Bulgaria (Evlogiev, 2007) (Fig. 1b). The area is characterized by undulating relief with an overall amplitude of up to 100 m, cut by deeply incised old river valleys (~50 m of incision), having generally a north-south orientation. The terrain is typical karstic with low groundwater table.

The studied Quaternary loess sequence lays on kaolinic clays deposits filling karstic depression developed in Low Cretaceous limestones. Fragmentary gravel beds are also present below the loess complex. The total thickness of the Kaolinovo's loess-paleosol sequence is 23.4 m exposed in an open pit quarry exploited for kaolin extraction (Figs. 1S, 2S and 3S from Supplementary information). It consists of seven loess horizons (L_1 to L_7 from top to bottom), interbedded by paleosol complexes numbered according to the European loess stratigraphic scheme (Marković et al., 2015). In the present study we focused on the uppermost 12 m deposits, covering the Holocene soil at the top (S_0), first loess L_1 , first paleosol S_1 , second loess L_2 , second paleosol S_2 , the third loess L_3 , and the paleosol complex below (S_3 and S_4).

Present-day climate is warm oceanic (Cfb) according to the updated Koppen-Geiger climate classification (Peel et al., 2007). According to the long term meteorological data from nearby meteorological stations, mean annual temperature is 10.3 °C with monthly maximum in July–August and monthly minimum – in January–February. Mean annual precipitation is 575 mm, with maximum in May–June and minima in March and September (Fig. 4S).

Natural vegetation cover is mainly steppe – forest (Vassilev and Apostolova, 2013), represented by grasses, bushes and patchy forests, which cover the undulating landforms. Nowadays, agriculture in Shumen region covers 52% of the surface. According to the “Atlas of soils in Bulgaria” (Koynov et al., 1998), Podzolized Chernozems (Degraded Chernozems) are the main soil type around the quarry, classified as Phaeozems in WRB classification system (IUSS Working Group WRB, 2015).

3. Sampled sections

Two loess sections were sampled in the Kaolinovo quarry, one in 2011 and the other in 2017–2019.

3.1. 2011 sampling campaign

The first sampling campaign was carried out in 2011 on the north-facing wall of the Kaolinovo quarry (Fig. 1S). The samples were collected every 5 cm over the whole loess-paleosol complex, except within an inaccessible 3 m thick interval (between 13 and 16 m). The lower part of section (19–23.5 m depth) is composed of thick reddish paleosol complex, the oldest loess horizon L_7 and red clays overlaying the kaolinic clays below (Fig. 1S). Block samples from least weathered levels of the three uppermost loess horizons have been collected for luminescence dating (Balescu et al., 2020).

3.2. 2017–2019 sampling campaigns

In 2017–2019, continuous sampling at 2 cm resolution was performed along the south-facing wall of the quarry down to 12 m depth (Figs. 2S and 3S). Cleaning the outcrops was done by hand tools removing approximately 1 m thick layer to collect about 300 g of fresh material per sample. Detailed profile's description is provided in Table 1S.

4. Methods

4.1. Laboratory magnetic measurements

The samples were air dried in laboratory, gently crushed and passed through a 2 mm sieve. Magnetic susceptibility of the bulk material was measured on MFK – 1 A susceptibility bridge (AGICO, Czech Republic) at 200 A/m field and two working frequencies – 976 Hz and 15,616 Hz. The material was filled into standard 10 cm³ plastic cylinders. Low-field mass specific magnetic susceptibility (χ) is calculated using sample's weight and the measured susceptibility at lower frequency. Frequency-dependent magnetic susceptibility χ_{fd} is calculated as the difference between the measured susceptibilities at low and high frequencies. This parameter is commonly used as an indicator for the presence of viscous superparamagnetic ferrimagnetic iron oxides (Dearing et al., 1996). Magnetic remanence measurements were performed on cubic samples (2×2×2 cm) prepared by mixing 2 g of dry powdered material with gypsum and water.

Anhyseretic remanent magnetization (ARM) was imparted using a Molspin AF demagnetizer with a 100 mT AF field superimposed on a 0.1 mT DC field. Isothermal remanent magnetization in 2 T field (IRM_{2T}) (considered as saturation isothermal remanence

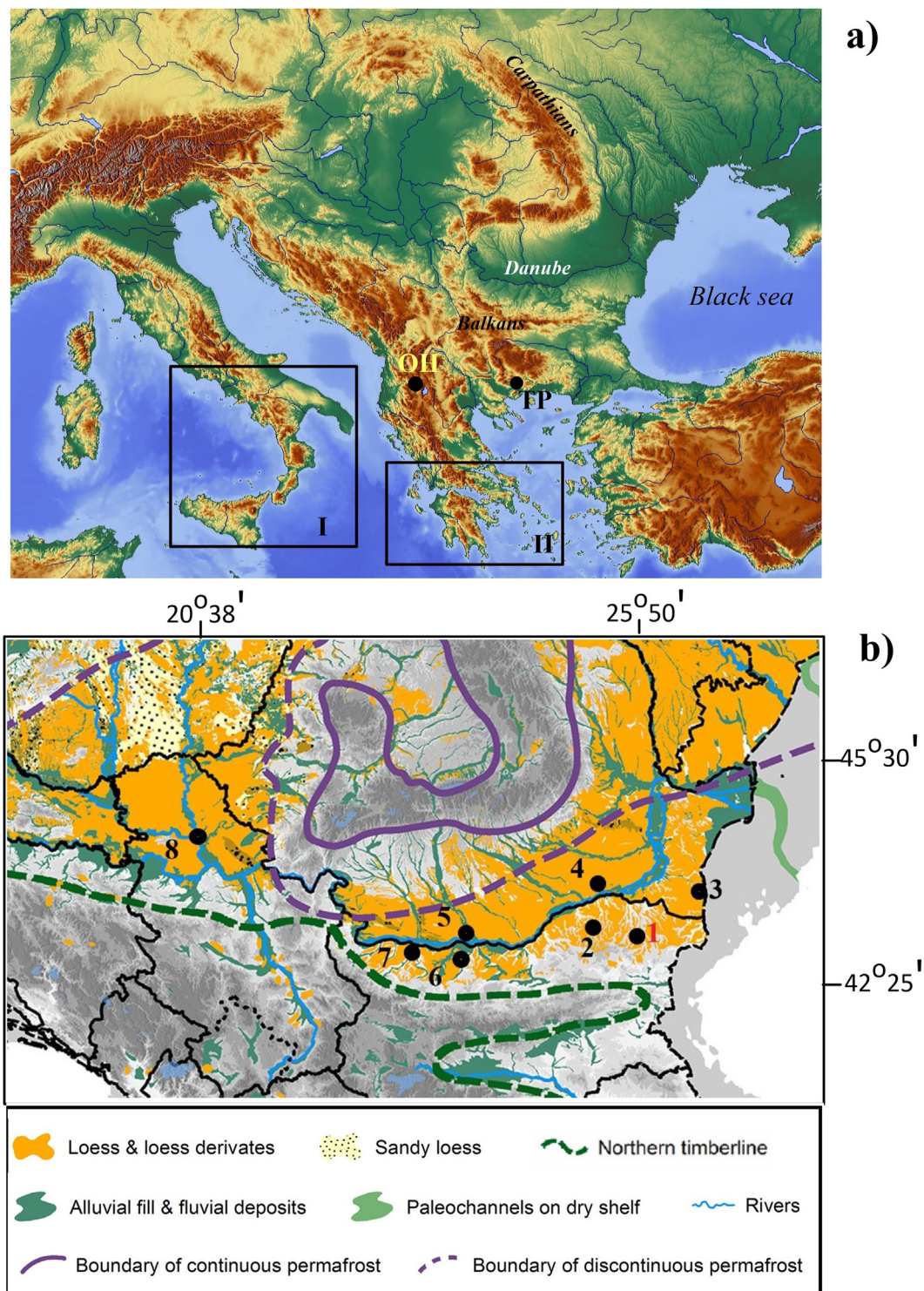


Fig. 1. a) Map of southeastern Europe with marked locations of lake Ohrid (OH) and Tenaghi Philippon (TP). Rectangles delineate the two major volcanic provinces – Italian (I) and Aegian (II). b) distribution of the loess cover in the study region (modified from [Lehmkuhl et al. \(2021\)](#)) and location of the loess-paleosol sequences discussed in the text: 1 – Kaolinovo (present study), 2 – Viatovo ([Jordanova et al., 2008](#)), 3 – Tuzla ([Balescu et al., 2003](#)); 4 – Mostistea ([Panaiotu et al., 2001](#)); 5 – Zimnicea ([Radan, 2012](#)); 6 – Pleven ([Jordanova et al., 2022](#)); 7 – Harletz ([Antoine et al., 2019](#)); 8) Stari Slankamen ([Song et al., 2018](#)).

magnetization) and subsequent –100 mT and –300 mT back fields have been acquired along the z-axis in IM-10-30 pulse magnetizer (ASC Scientific, USA). Magnetic remanences were measured on JR-6A automatic spinner magnetometer (AGICO, Czech Republic) with a sensitivity of 2×10^{-6} A/m. The S-ratio was calculated as:

IRM_{300mT}/IRM_{2T} ([Thompson and Oldfield, 1986](#)). High-coercivity remanence component HIRM was calculated according to [Robinson \(1986\)](#) as $0.5 \times (IRM_{2T} + IRM_{-300mT})$.

Magnetic hysteresis loops and back field remanence measurements were carried out for every second depth interval (number of

samples $n = 309$). VSM MicroMag 3900 instrument (Lake Shore Cryotronics, USA) was used with a maximum applied field of 1 T. Magnetic hysteresis parameters coercive force (B_c), saturation magnetization (M_s), saturation remanence (M_r), and high-field susceptibility (χ_{hf}) were calculated after correction for paramagnetic contribution of the high field ($H > 0.8$ T) portion of the loop. Coercivity of remanence (B_{cr}) has been obtained from back-field remanence measurements. Stepwise IRM acquisition up to 1.5 T field has been performed on 40 samples, for which grain size and geochemical analyses are also done. The curves of IRM acquisition were fitted by best-fit combination of log-normal distributions using the MaxUnMix software (Maxbauer et al., 2016). The main parameters determined are: the mean coercivity of an individual component (B_h), the component saturation magnetic remanence (M_r) as percent from the total remanence, and the dispersion parameter (DP) given by one standard deviation in log space.

Stepwise thermal demagnetization of composite remanence induced along the 3 sample's axes was used as a diagnostic tool for determination of coercivity and unblocking temperatures (T_{ub}) of the major magnetic remanence carrying minerals. The composite remanence was acquired consecutively with IRM_{2T} induced along + z axis; IRM_{0.2T} induced along + y axis; and ARM induced along + x axis. The resulting three orthogonal remanence components are: IRM_{0.2–2T}; IRM_{0.1–0.2T}, and ARM (acquired in maximum AF field of 0.1 T). The thermal demagnetization of this composite remanence was carried out at 19 steps starting from room temperature up to 700 °C in air using a MMTD shielded furnace (Magnetic Measurements, Ltd.; UK). Remanence signal was measured at room temperature after each heating step. The total intensity of each component is represented as a sum of several mineral – specific components, carried by different (ferro)magnetic minerals. These were identified by the observed remanence unblocking temperatures T_{ub} (see part 5.1.). Identified T_{ub} s suggest that ARM is carried by magnetite (mgt) and maghemite (mht) in various proportions. In few levels final T_{ub} of 700 °C of the ARM component point to hematite (hmt) contribution as well. Mineral – specific components building up IRM_{0.2–2T} and IRM_{0.1–0.2T} were determined in a similar way. An example with schematic representation of the approach is given in Fig. 5S.

The origin and type of magnetic minerals carrying the laboratory induced magnetic remanences were deduced by coeval analysis of the fitted components of IRM acquisition curves and thermal demagnetization of composite remanence.

4.2. Pedological analysis

Pedological analyses were performed on 34 samples at the INRAE soil analysis laboratory (LAS, Arras, France). They consist of: (i) particle-size distribution by wet sieving and pipette method (NF X 31–107); (ii) soil organic carbon (SOC) and total N concentration by dry combustion (NF ISO 10694); (iii) CaCO₃ concentration by volumetric method (NF X 31–106); (iv) total Fe (Fe_{tot}) concentration by ICP-AES measurements after dissolution with hydrofluoric and perchloric acids (NF X 31–147); (v) Fe concentration measured by ICP-AES after extraction by the dithionite-citrate-bicarbonate method (Mehra-Jackon, 1960), a proxy of total iron oxides in soils (Fe_d); Fe concentration measured by ICP-AES after extraction by the oxalate method (Tamm, 1922), a proxy for poorly crystalline iron oxides in soils (Fe_o). Cation exchange capacity (CEC) was measured by the cobaltihexamine chloride method (NF X 31–130).

Based on particle size data, the Coarse Silt Index (CSI) defined by Schirmer (2016) and the Grain Size Index (GSI) defined by Rousseau et al. (2002) were calculated as follows:

CSI = coarse silt/fine silt

GSI = coarse silt / (clay + fine silt)

where coarse silt is the fraction (20–50 μ m); fine silt (2–20 μ m), and clay (<2 μ m).

4.3. Statistical analysis

Principal component analysis (PCA) was performed separately on three sets of data:

- i) intensities of the remanence components carried by different iron oxides, identified by 3-axis composite remanence thermal demagnetization, and components determined from IRM acquisition fits for a set of 40 samples. The input variables for the PCA analysis were chosen as follows: mean coercivity B_h of each fitted IRM component (Bh-C1, Bh-C2, Bh-C3, Bh-C4); the corresponding relative share of the four IRM components unmixed (C1%, C2%, C3%, C4%); intensities of ARM carried by magnetite and maghemite (ARMmgt + mht); intensities of IRM_{0.1–0.2T} (depicted as IRMs) carried by magnetite and maghemite (IRMs mgt + mht); intensity of IRMs carried by hematite (IRMs hmt); and intensities of IRM_{0.2–2T} (depicted as IRMh) carried by maghemite (IRMh mht) and hematite (IRMh hmt). The intensities of ARM and IRMs, carried by strongly magnetic magnetite and maghemite are summed up due to their similar magnetic characteristics and coercivities, which cannot be discriminated by unmixing IRM acquisition curves. The observed unblocking temperatures were not included in the analysis as they are discrete variables. All variables were standardized to have zero mean and a standard deviation of one.

- ii) magnetic parameters measured for the 309 samples along depth of the profile. The following set of 16 magnetic parameters and ratios were included in the analysis: χ , χ_{fd} , $\chi_{fd}^{\%}$, ARM, M_s , M_r , HIRM, IRM_{2T}/ χ , χ_{fd} /HIRM, ARM/IRM_{100mT}, χ_{ferri} / M_s , B_c , B_{cr} , S-ratio, M_r/M_s , B_{cr}/B_c .

- all pedologic parameters for a set of 35 samples.

Statistical analyses were performed using Statistica 10 (StatSoft Inc.) and xlstat packages.

5. Results

5.1. Mineral magnetic carriers

5.1.1. Acquisition of isothermal remanent magnetization (IRM) and unmixing of coercivity components

The choice of coercivity components' number assumes that the bulk signal of the samples from (paleo)sol units is composed at least by two medium coercivity components, representing detrital and pedogenic strongly magnetic fractions. A third component should reflect the presence of high-coercivity weakly magnetic phases and, another (fourth) component could be used in fitting the curves at low fields, where we expect the signal from viscous ferrimagnetic grains. Using this approach, most of the IRM acquisition curves are fitted by four components, with exception of several levels from the upper 5 m of the profile, spotting loess material from L₁ and L₂. Examples for the shapes of typical IRM acquisition curves and the fitted components are given in Fig. 6S. The softest coercivity component (C1) is characterized by low B_h values of 4–9 mT, contributing 1–15% to the total remanence with higher share in paleosol horizons and notable increase at 580–1176 cm depth. The association of high C1 intensity with paleosols suggests that probably C1 originates from pedogenic SP-

viscous SD fraction. In support of such supposition is the observed relationship between the intensity of the C1 component and frequency dependent magnetic susceptibility (χ_{fd}) (Fig. 7S). The correlation is relatively weak and this could be due to possible contribution of multidomain grains to C1, as well as larger experimental errors in IRM measurements at low DC fields (Roberts et al., 2019). Another source of uncertainty may come from the type of the fitting function used (He et al., 2020). The second component (C2) has mean coercivity in the range 15–23 mT and varying contribution (from 20 to 55%) to the total magnetization. The third IRM component (C3) presents a mean B_h value in the range 30–80 mT and contribution between 30 and 70% to the total IRM intensity. High coercivity component (C4) contributes between 3 and 15% to the total IRM and its mean coercivity strongly changes with depth – from (650–1800) mT in the upper 6 m to (115–560) mT in the lower part of the profile (6–12 m). Numerical values of the fitting parameters for the samples shown in Fig. 6S are presented in Table 2S.

5.1.2. Stepwise thermal demagnetization of composite remanence

The three orthogonal components reveal different unblocking temperatures (T_{ub}) during stepwise thermal demagnetization experiments (examples are given at Fig. 8S). The ARM component shows progressive demagnetization which is unblocked at final T_{ub} of 580 °C except in B₂, B₃ and B/C horizons of paleosol S₂ and B₃ of S₃ where T_{ub} of 400–450 °C are observed. A different demagnetization behavior is typical for the IRM_{0.1–0.2T} component (designated IRM_s) (Fig. 8S, middle column). Large part of the remanence is sharply unblocked around 250–300 °C. The remaining magnetization then continuously decreases until 700 °C in most samples. The high coercivity component – IRM_{0.2–2T} (named IRM_h) as remanence signal remaining along the +z axis after consecutive applications of DC fields of 2 T along +z axis and 0.2 T along +y axis – shows similar demagnetization behavior with a higher proportion of remanence unblocked at 700 °C. According to Dunlop and Ozdemir (1997), T_{ub} of 580 °C is ascribed to magnetite, T_{ub} of 270–350 °C to maghemite – hematite transformation during heating, and T_{ub} of 700 °C to hematite. We consider the observed T_{ub} of 250 °C on the IRM_h component as representing maghemite as well.

Thus, diagnostic mineral magnetic experiments point out to the presence of strongly magnetic magnetite and maghemite with

wide grain size distributions, contributing to coercivity components C1, C2 and C3. Hematite is also identified, being involved not only in the high – coercivity fraction, saturated in fields higher than 200 mT, but also is present as low-coercivity fraction, saturated in the field range 100–200 mT.

5.1.3. PCA on remanent components carried out by different iron oxides

The results from the PCA analysis show that 67.5% of data variance is explained by the first two components (Fig. 2). The first component F1 accounts for 43.4% of the total variance and F2 for 24.1%. Fig. 2a shows the projection of variables on F1 x F2 plane. The first component F1 is strongly positively correlated to C3%, IRM_{s-hmt}, C1%, C4% and IRM_{h-hmt}. At the same time, F1 is negatively correlated to the mean coercivity of C3 component (B_h -C3) and the percent contribution of C2 (C2%) (Fig. 2a). The second principal component F2 is mainly correlated positively to ARM_{mgt + mht} and negatively correlated to C3%. The observed sample positions in F1 x F2 components space reveal firm discrimination among different units (Fig. 2b). With respect to F1, mineralogy of the lower part of the profile (loess L₃, the deposits below described as A-horizon of S₄ and the soil S₃) is significantly different from the magnetic minerals from loess units L₁ and L₂, and the upper (paleo)sols S₀, S₁ and S₂. With respect to F2 component we see clear sub-division between loess and (paleo)sols (Fig. 2b).

Depth variations of F1 and F2 along with the corresponding variables, having the highest loadings are depicted in Fig. 3a and b. The major shift in F1 observed at 778 cm depth corresponds to the increase in the intensity of IRM_{h-hmt} and systematically lowered contribution of C2%. F2 component discriminates between loess horizons and paleosols S₁ and S₂. Variability in the examined data set not explained by the first two components is mainly related to the coercivity of the softest IRM component (B_h -C1) and intensity of the IRM_s component, carried by hematite (IRM_{s-hmt}). Their variations with depth are shown in Fig. 3c. Systematically higher intensities of IRM_{s-hmt} start to appear after 7 m depth accompanied by significant drop in coercivities of C2 and C3 components (Fig. 3d).

Thus, F2 component comprises the effect of pedological variability (e.g. loess vs paleosol) with higher maghemite fraction in paleosols as compared to loesses. The first component F1, which accounts for the largest part of data variability, subdivides the

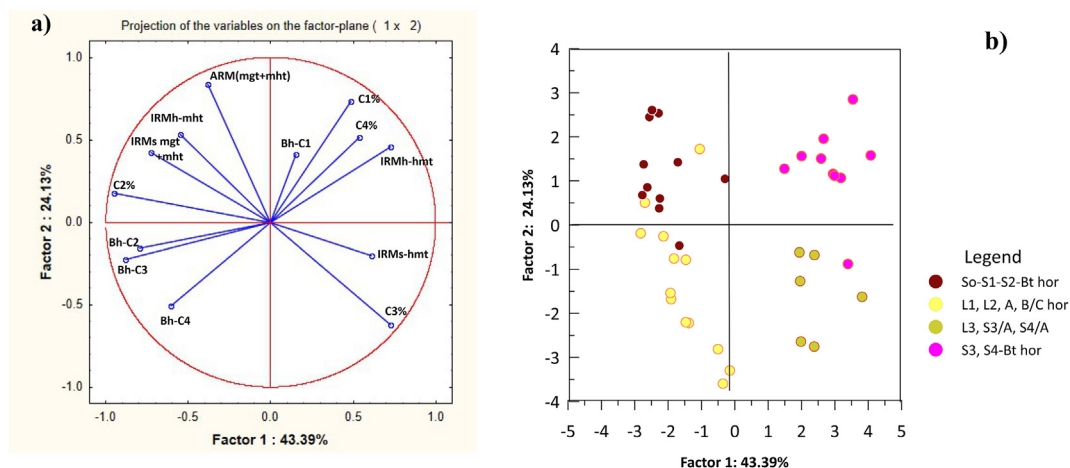


Fig. 2. PCA results for remanence components carried out by different iron oxides. a) circle of correlations for the first two principal components; b) projection of cases on the factor plane F1 x F2. The distribution of samples in the F1 x F2 space shows clear grouping: yellow color – area of loess samples and samples from A- and B/C horizons of S₀, S₁ and S₂ paleosols; brownish color – samples from loess L₃, A-horizon of S₃ and S₄ paleosols; pink color – area of samples from B- horizons of S₃ and S₄ paleosols; brown color – samples from B-horizons of S₀, S₁ and S₂ paleosols. (For interpretation of the references to color in this figure legend, the reader is referred to the Web version of this article.)

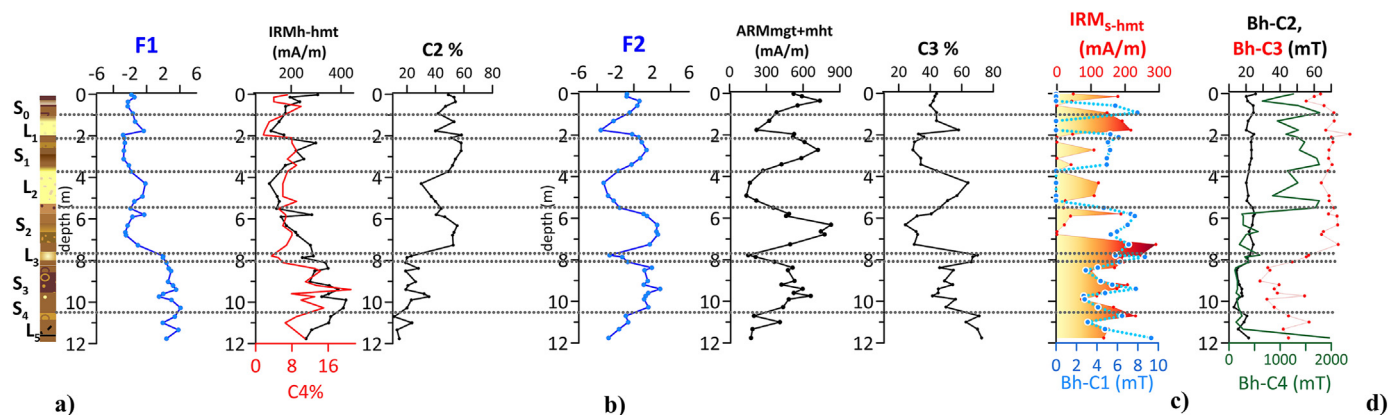


Fig. 3. Depth variations of a) the PCA component F1 and the two variables with the highest contribution to F1 – IRMh-hmt, C4% /red/ and C2%; b) the PCA component F2 and the variables with the highest contribution to F2 variability – ARMmgt + mht and C3%; c) the intensity of low-coercivity hematite component (IRMs-hmt) and coercivity of component C1 (Bh-C1); d) the estimated mean coercivities of IRM components 2, 3 and 4 (Bh-C2 /black line/, Bh-C3 /red/ and Bh-C4 /grey/). (For interpretation of the references to color in this figure legend, the reader is referred to the Web version of this article.)

profile in two contrasting parts with respect to the amount and coercivity of hematite, which is probably related to change in parent loess mineralogy and can be considered as a lithological effect.

5.2. High-resolution depth records of rock magnetic parameters

Concentration-dependent magnetic parameters such as magnetic susceptibility (χ), frequency-dependent magnetic susceptibility (χ_{fd}), ARM, SIRM show synchronous behavior with depth. These parameters are sensitive to the presence of ferrimagnetic fraction in typical domain states. Namely, the superparamagnetic (SP) fraction dominates in χ_{fd} , single domain/vortex state (SD/PSD) fractions - mainly control the ARM (Liu et al., 2012). Pronounced increase of these magnetic parameters are observed in all soils (Holocene soil and the three paleosols) (Fig. 9S) as generally observed in most loess-paleosol sequences (Evans and Heller, 2003; Marković et al., 2015; Maher, 2016).

A PCA analysis was performed on the high-resolution magnetic proxies to discriminate different pedologic units and interpret the observed depth variations. The results show that first two components account for 75% of the data variance with 64% of F1, and 17% of F2 (Fig. 4). Concentration – dependent magnetic parameters have the highest contribution to F1, influenced by the enriched strongly magnetic fraction formed *in-situ* during periods of enhanced pedogenesis. Among them, the highest loadings are coming from the magnetic parameters, sensitive to the presence of SP and SSD ferrimagnets (χ_{fd} , $\chi_{fd}\%$, χ_{ferri}/M_s , ARM) opposing to the similar contribution from coercive force (B_c), coercivity of remanence (B_{cr}) and the ratio IRM_{2T}/χ (Fig. 4a, Table 3S). The second component F2 is aligned with the ratios M_r/M_s and B_{cr}/B_c and opposes the S-ratio. The distribution of samples in F1 x F2 space is presented in Fig. 4b. Here, the first component F1 discriminates between loess units (aligned with B_{cr} , B_c and IRM_{2T}/χ vectors) and (paleo)soil samples from S_0 , S_1 , S_2 and $B_1 - B_3$ horizons of S_3 . The second component F2 reflects mainly the opposite behavior of S_3-B_4 , S_4-A and L_4 with respect to the loess and paleosol samples from the upper units (Fig. 4b). The first two principal components show depth variations, strongly related to the behavior of the variable, giving the highest contribution (Fig. 5a and b). The variability of F1 with the strongest amplitude is best modulated by magnetic susceptibility and coercive force (B_c) of the remanence carriers. The second component (F2) reveals depth variability intimately governed by the relative contribution of the high-coercivity

ferromagnetic fraction expressed by the S-ratio, and changes in the ratio M_r/M_s . This component shows systematic shift from positive to negative signal marked by the third loess (L_3) (Fig. 5b). Total variance of the data set, comprised by the magnetic parameters shown on Fig. 4a is guided by those sensitive to the presence of strongly magnetic iron oxides – magnetite and maghemite (Liu et al., 2012). However, even though possessing weakly magnetic signal, (antiferromagnetic) oxyhydroxides are also important environmental proxy parameters. Such a parameter is high-coercivity remanence (HIRM) (Fig. 5c). It shows higher values in three intervals corresponding to B_2 horizon of the Holocene soil (S_0), to all horizons of the S_1 paleosol, although HIRM values slightly decrease downward; and to the B_3 horizon of S_2 paleosol. Magnetic ratios M_r/M_s and B_{cr}/B_c derived from hysteresis measurements, the coercive force (B_c) and coercivity of remanence (B_{cr}) are utilized widely in classic rock magnetic studies as magnetic domain state and/or mineral sensitive parameters (Dunlop and Ozdemir, 1997; Liu et al., 2012; Roberts et al., 2018, 2019). The three loess horizons are characterized by higher B_c and B_{cr} with especially higher values within the L_2 loess horizon (Fig. 5). Similar relative increase in coercivities with maxima at 1180 cm depth, described as B_4 horizon of paleosol S_3 , suggests that this horizon corresponds to a non-fully pedogenized loess unit. Coercivity variations are similar to the ones expressed by the IRM_{2T}/χ ratio (graph not shown, see the close proximity of the three vectors in Fig. 4a).

5.3. Pedological parameters

Variability in pedological parameters, determined for 34 representative samples from each horizon described in the field, were analyzed by PCA. The 13 variables used for the statistical analysis are: particle-size fractions (as %): <2 μ m, silt, sand; the particle-size indexes GSI and CSI; $CaCO_3$, SOC, N_{tot} , the ratio C/N; CEC, total Fe (Fe_{tot}), crystalline Fe ($Fe_{crist} = Fe_d - Fe_o$), poorly crystalline Fe (Fe_o). The initial analysis on all samples reveals that the first two components explain 51.9% and 24.4% respectively of the variability in the data (Fig. 6a). The first component is positively correlated to silt and $CaCO_3$ content, and negatively correlated to the fraction <2 μ m, Fe_{crist} , and total iron Fe_{tot} (Fig. 6a). The second component is determined by the positive loadings of SOC, N_{tot} and Fe_o (Fig. 6a). Depth variations of the first two components along with their most contributing variables are presented in Fig. 7.

As far as the highest loadings in F1 and F2 discriminate generally among loess and paleosol samples, we carried out a second PCA on

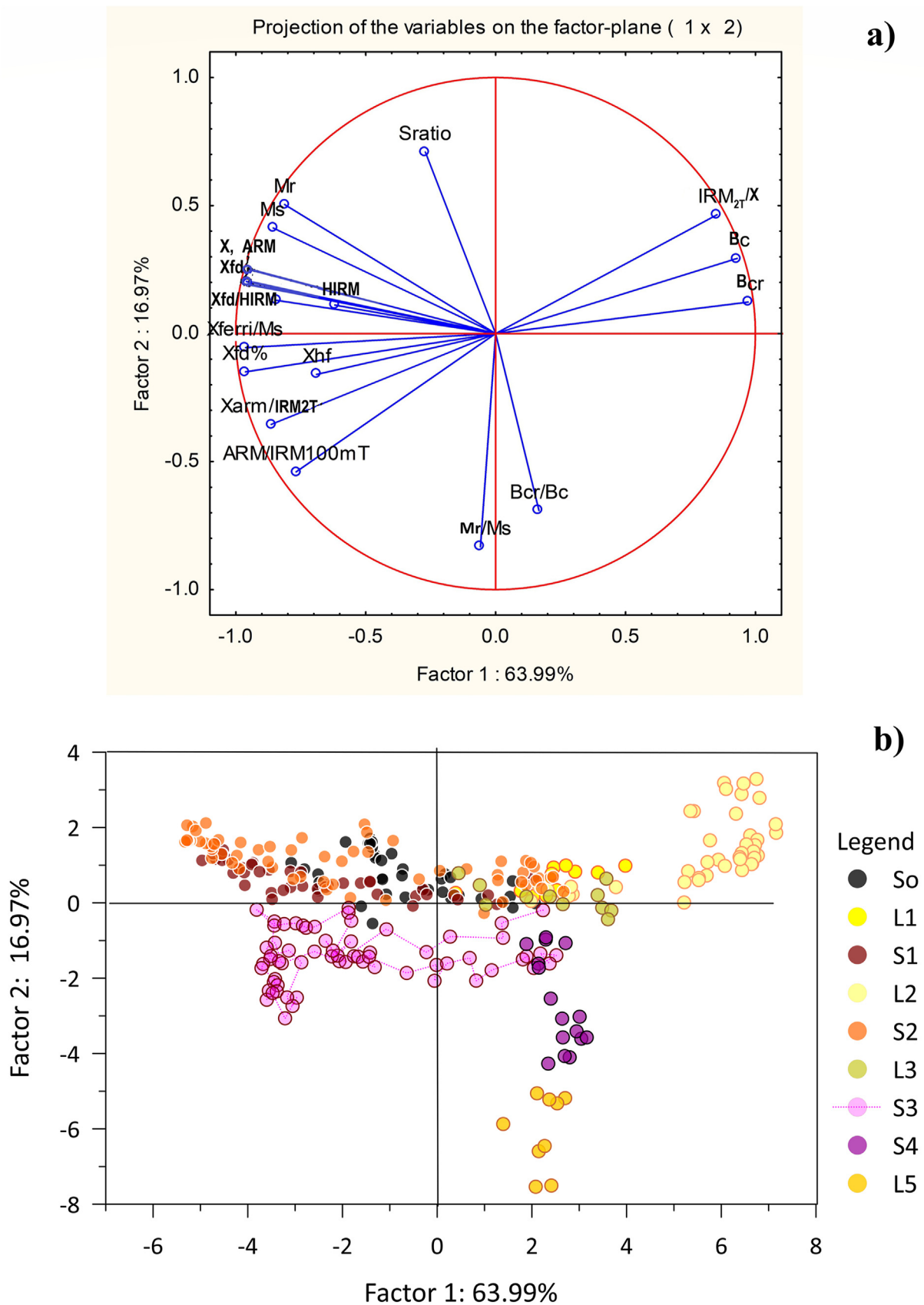


Fig. 4. PCA results on magnetic parameters and ratios. a) Circles of correlations of first two principle components F1 and F2; b) projection of samples on F1 x F2 plane. Symbols are colored according to the units: black – Holocene soil S₀; brown – S₁; orange – B and B/C horizons of S₂; orange – S₂; pink – S₃; violet – S₄; shades of yellow – loess samples. (For interpretation of the references to color in this figure legend, the reader is referred to the Web version of this article.)

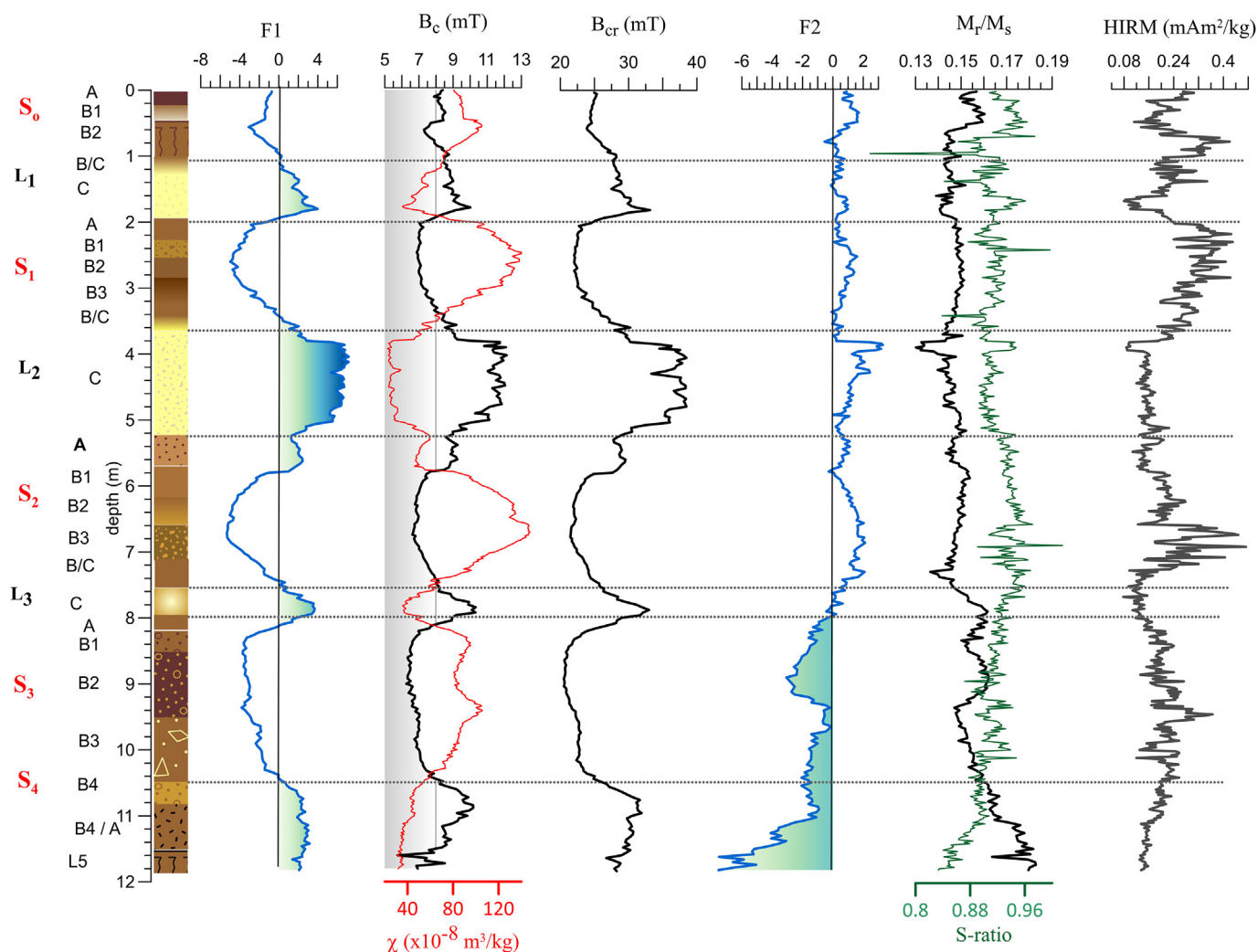


Fig. 5. Depth variations of factor coordinates of cases (samples) for component F1 and the variables with the highest contribution to F1 - coercive force (B_c), coercivity of remanence (B_{cr}) and magnetic susceptibility (χ); component F2 with its most contributing variables - S-ratio and M_r/M_s ratio; and hard isothermal remanence (HIRM) variability.

paleosol samples excluding the Holocene soil and the loess samples for a better discrimination between the paleosol horizons. The two first components of this second PCA explain 77% of the variance, with 50.5% and 27.2% of the variance for the first and second component respectively (Fig. 10S). The distribution of pedological variables in F1 x F2 space replicates the picture, obtained after inclusion of samples from loess horizons and S_0 . Consequently, the effect of changing SOC composition and stability with time (Sierra et al., 2018) for the “young” carbon pool is not the main source of variability. The samples from all horizons of paleosol S_1 are well distinguished from the rest in F1 – F2 space.

6. Interpretation

6.1. Sources, origin and evolution of magnetic signal along Kaolinovo profile

Variations in type and relative abundance of mineral magnetic phases show high dependence on profile's stratigraphy. The third loess (L_3 , 750–795 cm) is a critical boundary for all magnetic properties changes, particularly for the type and coercivity of mineral magnetic carriers. Magnetic properties above L_3 (S_0 , S_1 , S_2 and loesses L_1 and L_2) are significantly different from those in the

lower part of the profile (L_3 , S_{3-4}) as shown in Fig. 2b by the first PCA component. This is mainly controlled by variations in relative contribution of C2 component (Fig. 3a) along with changes in coercivities of the second and third IRM components up to 700 cm depth (Fig. 3d). Meanwhile, intra – parametric variations of Bh-C2 and Bh-C3 between loess and paleosols in the upper part of the profile (0–700 cm) are small (Fig. 3d). The largest differences are observed between the upper and lower parts of the profile, from (20–25) mT to (15–17) mT in Bh-C2 and from (55–65) mT to (30–45) mT in Bh-C3, respectively (Fig. 3d). The opposite behavior of C2% and C3% (Fig. 3 a, b) with highs and lows in paleosols (loess units) respectively suggests a pedogenic origin of C2% and detrital of C3%. On the other hand, the intensities of the high-coercivity hematite component (IRM_{h-hmt}) are not straightforwardly related to C2 or C3 relative shares. It resembles more C2 behavior in the upper 8 m and switches to C3 in the deeper horizons. In contrast, intensities of IRM_{s-hmt} (Fig. 3b and c) well resemble the changes in the relative share of the detrital C3 component. These relationships suggest detrital hematites as the mineral carriers of the C3 component. Lower coercivities and C3% increase indicates an overall increase in the amount of detrital hematites fraction within the 700–1200 cm interval due to change in the source material (Figs. 2a and 3a-b, d). Mean coercivities of the fourth high-

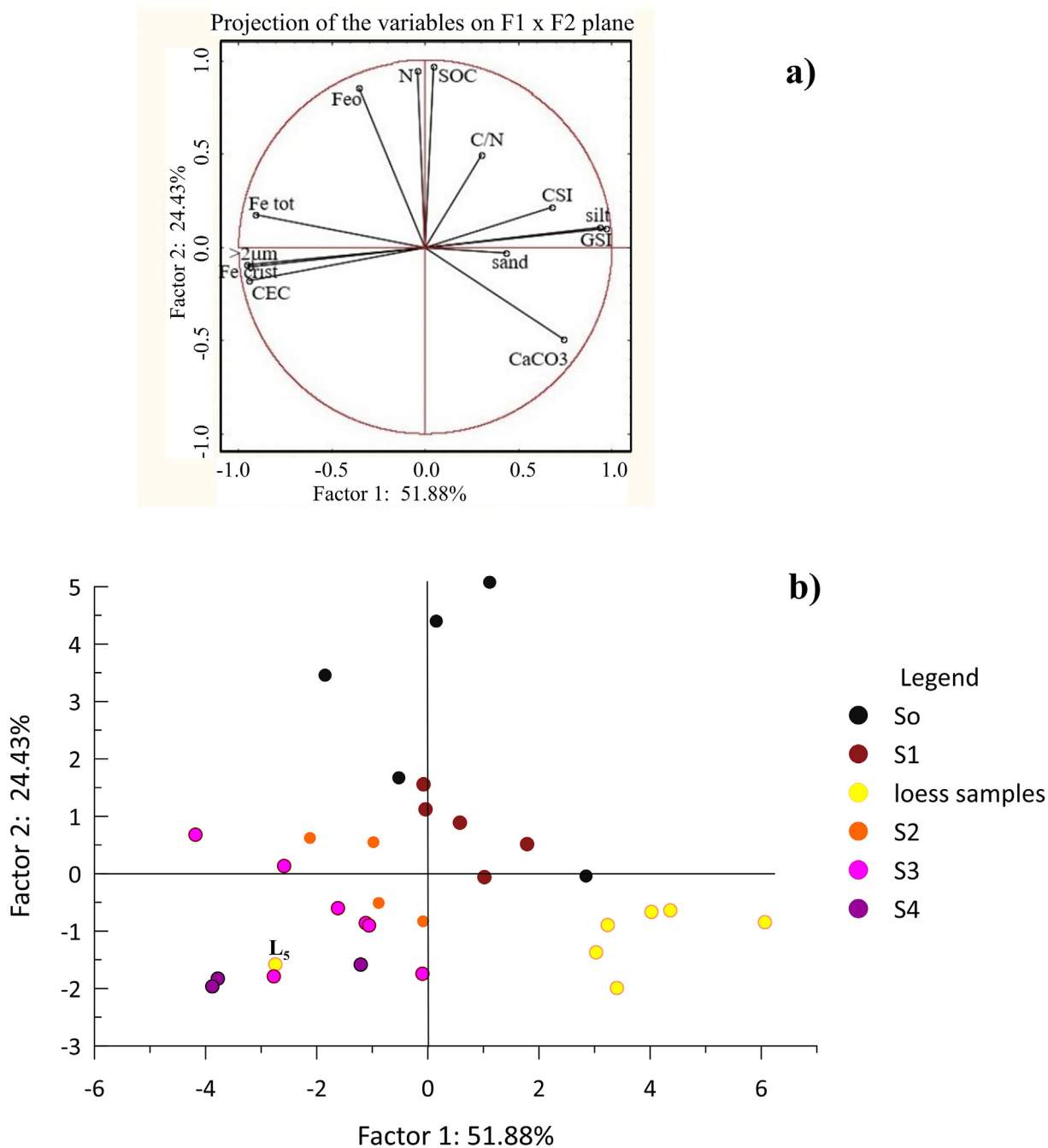


Fig. 6. PCA on pedologic variables. a) Circle of correlations of first two principle components F1 and F2; b) projection of samples on F1 x F2 plane. The distribution of samples shows clear grouping: area of loess samples marked by yellow color is shifted towards positive F1 loadings and negative F2 loadings; areas of distribution of the paleosol samples from different horizons of S₀, S₁, S₂, S₃ and S₄ are spread from positive (S₀) towards progressively more negative F1 and F2 loadings. (For interpretation of the references to color in this figure legend, the reader is referred to the Web version of this article.)

coercivity component C4 largely change from more than 1000 mT in the upper 6 m to about 100 mT in the interval 8–12 m (Fig. 3d). The C4% shows close relation with IRM_{h-hmt} (Fig. 2a), which significantly contributes to F1 component. We therefore propose that the C4 component represents pedogenically produced hematite, involved in IRM_{h-hmt} remanence.

Our interpretations suggest that the first component F1 reflects the interplay between the relative contribution of detrital hematites, associated with properties of the parent loess material, and pedogenically produced hematite, the latter being dependent on

the pristine loess mineralogy and grain size. The second principal component F2 (Fig. 3b) is positively correlated to the intensity of ARM_{mgt + mht} and negatively correlated to C3% contribution. Consequently, it points out the interactions between pedogenic formation of magnetite-like fractions, carrying ARM and low-coercivity hematite fraction in the parent loess (C3 component carrier). The lowest coercivity IRM component C1 is characterized by coercivities of 3–9 mT, typical for viscous SP magnetite particles of pedogenic origin (Eyre, 1996; Heslop et al., 2015). Its increase in the lower part of the profile (800–1200 cm) reflects the overall

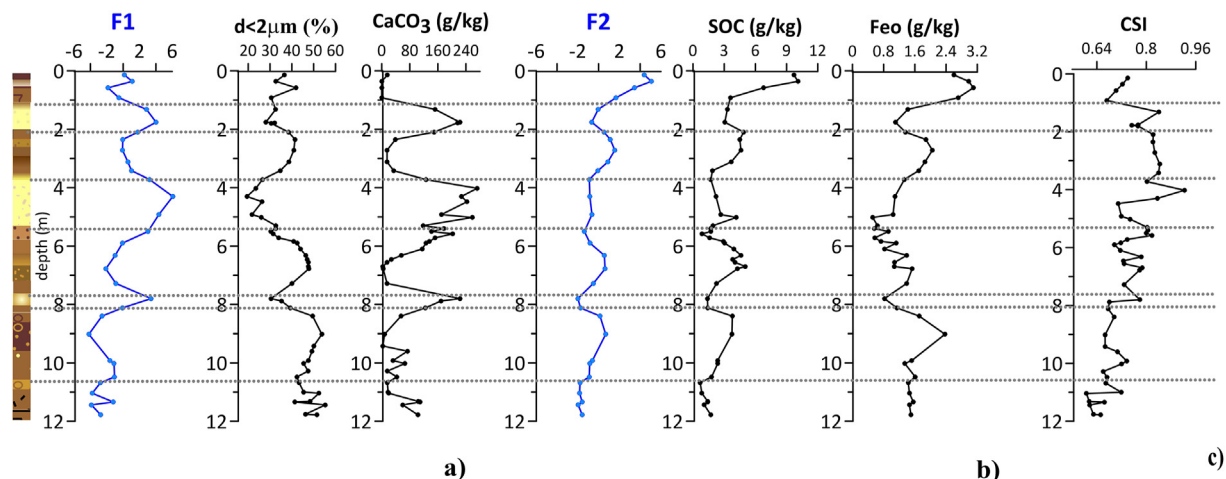


Fig. 7. Depth variations of a) the PCA component F1 on pedological variables and the two variables with the highest contribution to F1 – clay content ($d < 2 \mu\text{m}$) and CaCO_3 ; b) the PCA component F2 and the variables with the highest contribution to F2 variability – soil organic carbon (SOC) and poorly crystalline iron (Fe_o); c) the Coarse Silt Index (CSI).

lower coercivity magnetic minerals, both magnetites and hematites. Thus, our magnetic mineralogy results highlight the key role of parent material mineralogy and properties for *in-situ* formed pedogenic magnetic phases.

7. Discussion

7.1. Chronostratigraphy of the Kaolinovo profile

Magnetic susceptibility permits to correlate the two parallel profiles from the 2011 and 2017/19 campaigns using the low χ values from the upper three loess horizons L_1 , L_2 and L_3 , and the enhanced χ values in paleosol horizons (Fig. 8). Three post-infrared infrared (PIR-IR) ages were obtained on K-feldspar grains from the three upper loess horizons (L_1 , L_2 , L_3) in the Kaolinovo 2011 sequence (Balescu et al., 2020). The depth levels corresponding to PIR-IR ages have been transferred from the 2011 profile to the 2017/19 using χ variations between loess and soil horizons. The stratigraphic position of the L_1 age corresponds to the local χ minimum at 1 m depth in the record from 2017/19 profile (Fig. 8). The sharp increase of χ within L_2 related to the cryptotephra layer is considered a secure mark for transferring the L_2 age. Similarly, least weathered material of 2011 profile from L_3 (lowest χ signal) is correlated to the corresponding lowest χ values in the 2017/19 profile.

The PIR-IR age (45 ± 2 ka) in the L_1 loess horizon (Balescu et al., 2020) suggests a deposition of its uppermost part during Marine Isotope Stage (MIS) 2. This implies a deposition of the lower part of L_1 during MIS4 which is consistent with the absence of a well-defined horizon with enhanced magnetic properties that could correspond to MIS3 within L_1 (Fig. 9S). The age in the second loess L_2 (167 ± 7 ka) ascribes it to MIS6. The age within the L_3 loess (296 ± 17 ka) advocate for a deposition during the MIS 8 interval.

The loess – paleosol sequences from the Viatovo quarry (Jordanova et al., 2008), as well as the Zimnicea borehole (Radan, 2012) and Tuzla section (Balescu et al., 2003) from the nearby Romanian plain (for location of the sites see Fig. 1b) provide a useful age constrain thanks to the identification of the Matuyama – Brunhes (M/B) geomagnetic field reversal in the seventh loess unit (L_7). The stratigraphic position of the M/B boundary along with the known lock-in-depth problem with geomagnetic field reversal records in loess-paleosol sequences (Spassov et al., 2003) implies a L_7 formation during MIS 20 (Fig. 8). The fourth loess L_4 is regionally

represented by very thin deposit or is generally absent as in the Viatovo quarry where its position corresponds to a massive hard layer of CaCO_3 concretions. Similarly, a layer of massive hard CaCO_3 concretions was described in the Kaolinovo profile at depth interval 950–1044 cm (see Table 1S and dashed line in Fig. 8). We thus interpret this interval as the remnants of L_4 deposited during MIS10 which implies that the lower lying B_4 horizon of the S_3 paleosol correspond to MIS 11. Accepting such a stratigraphic scheme, the oldest part of Kaolinovo (2017) profile (depth interval 1040–1140 cm) should conform to MIS12 (e.g. ~ 450 ka).

7.2. Change in eolian dust sources

The major source of low Danube loess is the alluvium of the Danube river (Lehmkuhl et al., 2021). Several authors also propose dust sources from the eastern/northeastern sector. According to Buggle et al. (2008), Ukrainian glaciofluvial sediments constitute a second source for loess deposited in the lower Danube area. However, those sediments are generally coarse grained, which contradicts our observation of increased fine silt and clay content in L_3 and older units (Fig. 7a, c). Stephens et al. (2003) suggests Aral and Caspian sea arid lands as a source for aeolian dust entrainment and transport by easterly winds towards the Black sea. Jipa (2014) proposed Black sea shelf as sedimentary eolian source at low sea level stands during glacial periods. The presence of large dried areas, available for dust deflation, over the Black sea shelf is alleged during isolated Black sea periods. Recent study by Hoyle et al. (2021) on a 400 ka record from NE Black sea sediment core (DSDP site 379) reveals evidences from dinocysts and Sr isotopes that the Black sea was disconnected from the Mediterranean and Caspian seas during MIS4, MIS 8 and MIS10 glacials. This favors sediments from the Black sea shelf as a source for aeolian dust deposition inland and could explain the peculiar magnetic signature of loess units L_3 and L_4 (the latter identified by the remnant CaCO_3 level). However, further geochemical data are required to untangle sediments sources.

Loess horizons are characterized by clay ($< 2 \mu\text{m}$) content comprised between 20 and 30% (Fig. 7a). We attribute such unusually high clay content for loess units to the geographic position of the site located south of the Danube river which is the main source of dust supply in the region (Evlogiev, 2007; Buggle et al., 2008; Jipa, 2014). Similar high clay contents were also observed in the loess horizons of the nearby Viatovo quarry, situated 50 km

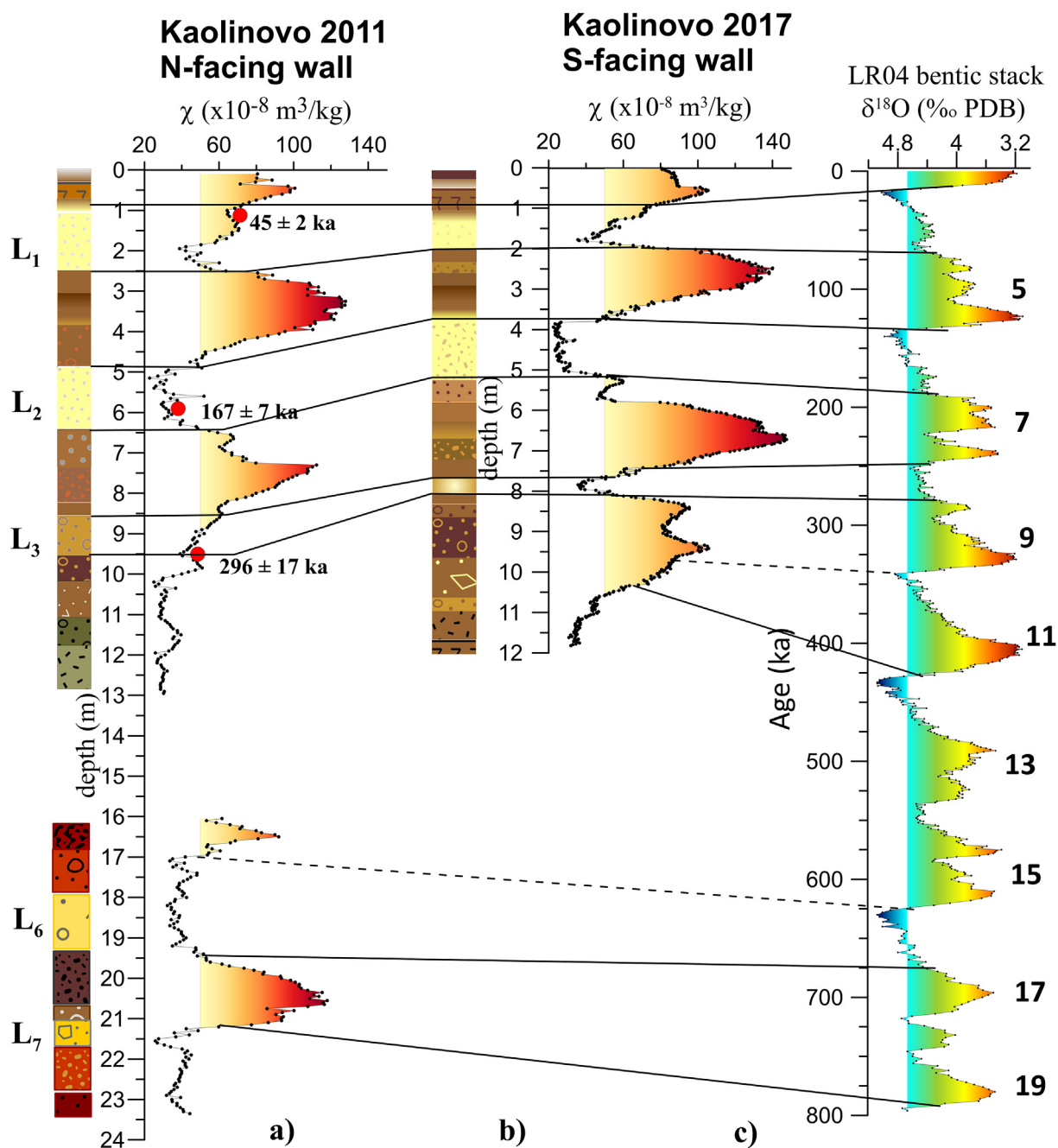


Fig. 8. Links between the two profiles sampled in 2011 (a) and 2017 (b) by using magnetic susceptibility variations with depth. Location of the samples from loess horizons L₁, L₂ and L₃ used for PIR – IR dating obtained by Balescu et al. (2020) are indicated; c) Links of magnetic susceptibility records with global stacked LR04 record of benthic ¹⁸O for the last 800 ka (Lisiecki and Raymo, 2005). Warm Marine Isotope Stages (MIS) (odd numbers) are indicated.

west from Kaolinovo (Jordanova et al., 2008) (Fig. 1b), and in the loess horizons L₁ and L₂ from a 40 km long N–S transect perpendicular to the Danube river at Pleven district (central North Bulgaria) (Evlogiev, 2007). In this regional transect, the clay fraction increases southward from 12 to 37% in L₁, and from 6–7 to 30% in L₂ supporting a dust fining with source distance. A particular feature of the bottom part of L₂ is the presence of a subdivision formed by the S₂-A horizon. No C-horizon was observed for the paleosol S₃. Instead, a less pedogenised horizon rich in silt and showing small increase in CaCO₃ content in S₃–B3 horizon (960–1020 cm) probably indicates a boundary between the welded S₃ and S₄ paleosols (see discussion in part 7.2.).

Variability in grain size fractions further reveal particular depth levels, which mark significant change in grain size distribution of the aeolian dust, persisting over certain depth intervals (Fig. 7a, c). The finest material is found within the deepest 4 m of the profile (800–1200 cm). The persistence of consistently high CSI values within S₁ paleosol and L₁ loess suggests an increased wind intensity and severe glacial conditions during mid to late MIS 6 and MIS 4. Similar pattern was observed in other loess – paleosol records from Central and Eastern Europe (Fitzsimons et al., 2012; Sümegi et al., 2020), from the Ioannina basin, NW Greece, over MIS 6 (Wilson et al., 2021) or in Lake Ohrid record (e.g. Francke et al., 2016). Because the CSI is defined as a ratio of coarse to fine silt fractions, its

variations are not affected by changes in the clay fraction related to pedogenic alterations of the primary loess material. Therefore, the absence of relative CSI minima in the paleosol S₁ probably indicates that dust sedimentation had effectively ceased during MIS 5 interglacial. Persistently low CSI values and negative values of F2 component of the PCA on magnetic parameters (Fig. 5) below 800 cm depth suggest less severe climatic conditions during MIS 8 and 10 glacial periods. The limit of our record and age uncertainty prevent to strictly discuss MIS 12. Notable change of depositional settings deduced from CSI variability (Fig. 7c) occurs at the depth interval of the identified cryptotephra layer in L₂ loess. Its stratigraphic position above the dated L₂ interval (pIRIR₂₉₀ age of 167 ± 7 ka, Balescu et al., 2020) is consistent with the widely observed (crypto)tephra layer in the second loess horizon in loess-paleosol profiles from Central and Eastern Europe (Marković et al., 2015; Antoine et al., 2019; Jordanova et al., 2022). This observation of significantly different hydroclimatic regimes in the region between early (before ca. 162 ka) and mid to late MIS 6 (162–130 ka), with less wind/more rain and more wind/reduced rainfall, respectively, is coherent with previous observations associated with large-scale atmospheric and oceanic reorganizations (e.g. Margari et al., 2010; Roucoux et al., 2011; Wilson et al., 2021).

The third loess horizon L₃ identified at 750–790 cm is the thinnest of the whole sequence (40 cm thick) and shows the highest magnetic susceptibility among the sampled loess units. The minimum χ value is 36.9 10⁻⁸ m³ kg⁻¹ at 780 cm accompanied by relatively high clay content up to 30% (Figs. 5a and 7a). It is worth noting that L₃ likely deposited during the small amplitude MIS 8 glacial period (see LR04 on Fig. 8). This loess horizon marks the gradual change in prevailing magnetic mineralogy from low-coercivity magnetically “soft” hematite to increasingly higher proportion of strongly magnetic maghemite at the base of paleosol S₂ (Fig. 3) developed during MIS 7.

The absence of non weathered fourth loess horizon (L₄) suggests a very weak dust accumulation at Kaolinovo during MIS10, with subsequent complete assimilation of the loess material into soil developed during MIS 9 (S₃). Sole field evidence for loess accumulation is the presence of a layer of large CaCO₃ hard concretions. Better preservation of L₄ loess was seen in a nearby quarry in the area (some 2 km to the west from the studied site). Such missing, or very thin loess horizons corresponding to the glaciations during MIS10 and MIS 8, coincides with the missing or very weak expression of these glacial periods in different records across Europe (Hughes et al., 2019).

7.3. Pedogenic development influenced by changing interglacial environments

The main variability of the pedological parameters opposes clay enriched (paleo)sol horizons against silt-dominated loess horizons (Figs. 6a and 7a). The second component highlights SOC and poorly crystalline iron (Fe_o) in the Holocene soil S₀ (Fig. 6b). Similarity in the distribution of samples in F1 x F2 space before (Fig. 6b) and after removal of those belonging to the Holocene soil and the loess units (Fig. 10S) points out that SOC content has also the highest loading on F2 component for paleosols.

Incorporation of the magnetic data into analysis of paleosols development allows gaining further information on the paleoclimate's role in shaping their properties and pedogenesis during ancient interglacials.

The sharp change in coercivity of the C4 IRM component (Fig. 3d) at depth of 650 cm together with the weak local minimum seen in magnetic signature between B₂ and B₃ horizons of the

paleosol S₂, and abrupt change in HIRM values (Fig. 5) suggest that the lower part of S₂ belongs to a separate soil-forming period, while the uppermost horizons developed on new eolian sediments. Considering chronological constrains, we propose that the formation of the upper (B₁ and B₂) and lower (B₃ and B/C) horizons of S₂ occurred during MIS 7a-c and MIS 7e sub-stages, respectively (Figs. 8 and 9). The higher HIRM values observed in the B₃ horizon (Fig. 5) suggest that the two paleosol horizons have been formed separately, but subsequently merged into in a welded profile. This interpretation implies the presence of a discontinuity (hiatus) in the record corresponding to eolian deposition during cold MIS 7 d. Terrestrial records spanning MIS 7 environmental changes in western and central Europe, Turkey and Israel (Columbu et al., 2019) document the establishment of more arid conditions during MIS 7 d, potentially suggesting a short time interval of eolian deposition within S₂ paleosol. The transition between MIS 7 and the following Pleniglacial MIS 6 shows relatively weak magnetic enhancement and increased coercivities (Fig. 5) suggesting the possible development of an incipient soil as already reported in loess-paleosol records from Carpathian and lower Danube loess areas (Marković et al., 2009; Obrecht et al., 2019). Such an incipient soil could have developed during a short climate amelioration period at the inception of cold MIS 6 (pollen zone OD5 from Sadori et al., 2016; Wilson et al., 2021).

The increasing contribution of pedogenic hematite to the total signal in the lower part of the profile suggests that older interglacials were characterized by warmer climates. A similar regional interpretation was raised from the loess-paleosol profiles of Stari Slankamen (Serbia) and Mircea Voda (Romania) (Buggle et al., 2014; Necula et al., 2015).

The weathering degree of loess material resulting from climatic amelioration events (increased temperature and/or precipitation) are fingerprinted by the frequency dependent magnetic susceptibility and the values of bulk low field magnetic susceptibility. The first loess horizon L₁ deposited during the MIS 2–4 interval exhibits relatively higher magnetic susceptibility (compared to other loess horizons) slowly decreasing towards the base of the unit at 185 cm (Fig. 5). Signs of higher biological activity are also deduced from the abundant presence of crotonas, root channels and intermixing of the material from upper levels (see profile description in Table 1S). These could be caused by climate amelioration during MIS 3, which is not expressed regionally by mature soils, but rather as incipient soils (Marković et al., 2015; Zeeden et al., 2018). The second loess L₂ is characterized by relatively steady and lowest magnetic susceptibility values of the whole profile (Fig. 5). The mean value (22.7 10⁻⁸ m³ kg⁻¹) observed within the upper part of the unit (380–420 cm) is the lowest in the studied sequence, suggesting low weathering of aeolian dust during the Penultimate glacial (MIS 6). Similar results, pointing to increasing wind intensity towards mid to late MIS 6 are reported by Sümegi et al. (2020) for Udvari core (SW Hungary), suggesting that this is a common feature on a regional scale. Stronger westerly winds associated with lower temperatures and reduced rainfall in the region could be induced by a southward migration of the winter polar front during glacial (or stadial) periods as already pointed out from Black Sea sediments (Wegwerth et al., 2016).

7.4. Kaolinovo mineral magnetic record as potential archive of tephra additions and their role for paleosol development

Fig. 9 shows magnetic susceptibility record along Kaolinovo profile together with the available age constrains from PIR-IR dating (Balescu et al., 2020); depth variations of magnetic

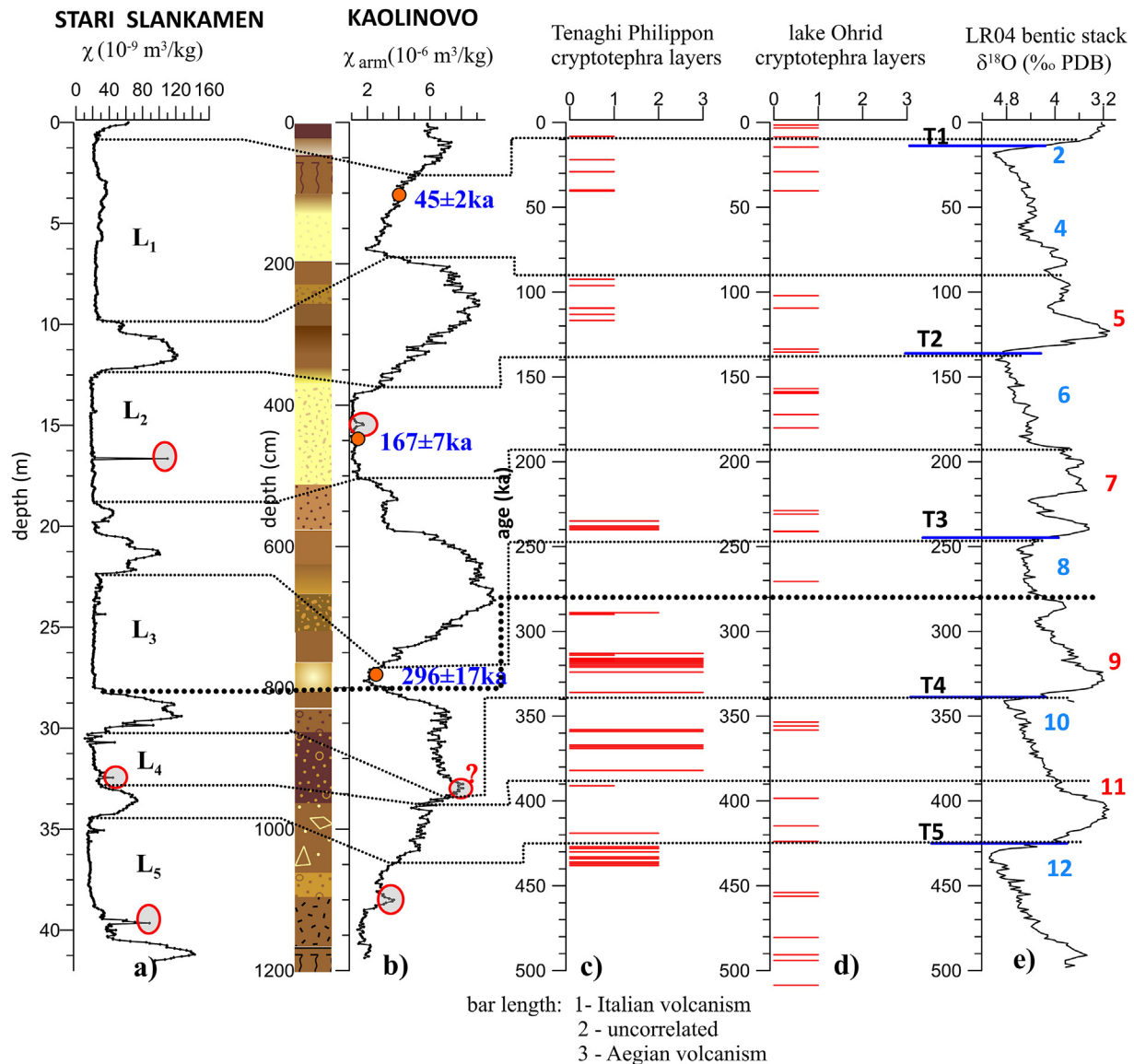


Fig. 9. Links between Kaolinovo record and Stari Slankamen loess-paleosol stack of Serbian loess (Song et al., 2018), identified tephra and cryptotephra layers in sediments from lake Ohrid (Leicher et al., 2019), Tenaghi Philippon (Vakhrameeva et al., 2018; 2019; Wulf et al., 2018), and LR-04 stack of Lisiecki and Raymo (2005). Marked by filled red circles levels from Kaolinovo profile are supposed to represent cryptotephra levels. Marked levels from Stari Slankamen record indicate depth intervals with described by the authors (Song et al., 2018) tephra layers. (For interpretation of the references to color in this figure legend, the reader is referred to the Web version of this article.)

susceptibility along Stari Slankamen stacked record from Serbian loess (Song et al., 2018); dated cryptotephra layers from lake Ohrid (Leicher et al., 2019) and Tenaghi Philippon (Wulf et al., 2018; Vakhrameeva et al., 2018; 2019), and the global $\delta^{18}\text{O}$ benthic stack (LR04; Lisiecki and Raymo, 2005).

The weak expression of MIS 10 and MIS 8 in Kaolinovo profile is accompanied by subtle irregularities or sharp peaks in magnetic susceptibility variations (marked by filled red ellipses in Fig. 9). These particular features are not related to measurements' uncertainties but are reflected in different magnetic parameters (χ , ARM, IRM and the ratios ARM/IRM_{100mT} as well as χ/M_s). Recent detailed study on loess-paleosol sequence from central north Bulgaria (Jordanova et al., 2022) revealed that depth variations of anhysteretic remanence (ARM) (resp. anhysteretic susceptibility χ_{arm}) is the most sensitive magnetic parameter with respect to identification of tephra additions into loess material. Several sharp peaks although not so intense, in χ_{arm} variability along Kaolinovo

profile are also identified (Fig. 9). We suggest that they correspond to a record of tephra additions into the eolian sediments, resulting in the formation of cryptotephra layers. These depth intervals have similar stratigraphic position within the profile as the occurrences of tephra layers within Stari Slankamen loess-paleosol stack from the middle Danube basin (Song et al., 2018). These layers were described as tephra by Song et al. (2018) and exhibit clear peaks in magnetic susceptibility record (Fig. 9a). Similarly, Panaiotu et al. (2001) and Balescu et al. (2010) report the presence of tephra layer in the second loess L₂ at Mostitea loess-paleosol profile. On Bulgarian territory, a visible tephra layer in L₂ was detected only in Suchia kladenetz quarry near Pleven (Jordanova et al., 2022), while at Harletz (Antoine et al., 2019) as well as at Kaolinovo (the present study) it is only identified as cryptotephra layer due to the larger distance to major volcanic provinces from the Mediterranean basin (Fig. 1a). Dated cryptotephra layers for the last 500 ka from two terrestrial archives in the Balkans – lake Ohrid (Leicher et al., 2019)

and Tenaghi Philippon (Philippi peatland, Greece; Wulf et al., 2018; Vakhrameeva et al., 2018; 2019) are also presented on Fig. 9. They show the occurrence of volcanic ash falls. A particularly large number of tephra and cryptotephra layers are reported for Tenaghi Philippon in the interval MIS 7c – MIS 12. We suppose that lower part of the Kaolinovo sequence (800–1200 cm, e.g. L₃, S₃–S₄) may be also affected by these frequent additions of volcanic ashes, which exert strong influence on mineral magnetic carriers and pedologic characteristics of these units. The incorporation of volcanic ash material in soil results in fast weathering of the glassy material and production of increased amounts of amorphous iron oxides, allophane, imogolite and halloysite clay minerals (Quantin et al., 1988; Joussein et al., 2005; Cravero and Churchman, 2016). Our data of amorphous iron oxides suggest increased amounts of Fe_o at 900 cm depth, corresponding to S₃–B2 horizon, which shows anomalous magnetic signature (see above). Moreover, additional inputs of poorly crystalline Fe oxides (ferrihydrite) and leached Al from volcanic ash weathering represent favorable conditions for precipitation of Al-substituted hematites in warm climates (Schwertmann et al., 1979; Lewis and Schwertmann, 1979; Cornell and Schwertmann, 2003). Tsai et al. (2010) also show that increasing temperature lead to transformation of metastable poorly crystalline materials (e.g. allophane, ferrihydrite) into thermodynamically more stable minerals (e.g. kaolinite, hematite) within volcanic ash material in soil.

8. Conclusions

Multi proxy analysis of combined magnetic and pedological properties along Kaolinovo loess-paleosol profile reveals that such an approach provides detailed information on the interplay between loess sedimentation and pedogenesis. Mineral magnetic and rock magnetic data successfully disentangle the response of pedogenic mineral transformations and weathering to changes in source material and the texture of the parent loess (e.g. grain size distribution), climate and possibly can identify intervals with additions of volcanic ash particles. We demonstrated that the incorporation of a detailed analysis on the type and coercivities of mineral magnetic remanence carriers is a powerful tool for revealing changes in the dust source and the relative importance and interplay between aeolian dust deposition and pedogenesis. Moreover, we show that using PCA in the analysis of magnetic data is a robust approach for discriminating the roles played by various environmental factors on the formation of the bulk signal. Depth changes in concentration dependent magnetic parameters (χ , χ_{fd} , ARM, IRM_{2T}) reflect the content of strongly magnetic magnetite/maghemite carriers, clearly distinguishing non weathered loess from pedogenized units. On the other hand, pedological parameters discriminate paleosols from loess units through opposing silt – dominated texture classes in loess to clay – dominated paleosol horizons. Thus, concentration changes of strongly magnetic iron oxides along loess-paleosol sequences can be considered as proxies for relative variations in sedimentary texture, e.g. silt to clay fractions.

CRedit statement

Diana Jordanova (DJ) - Original Draft Preparation, Conceptualization, Formal analysis, Supervision, Funding acquisition, Project administration. Quentin Simon (QS) - Writing - Review & Editing, Conceptualization. Sanda Balescu (SB) - Investigation, Writing - Review & Editing. Neli Jordanova (NJ) - Writing - Review & Editing, Visualization, Conceptualization. Daniel Ishlyanski (DI) - Investigation, Formal analysis. Bozhurka Georgieva (BG) - Investigation, Formal analysis. Didier Bourlès (DB) - Conceptualization. Adrien

Duvivier (AD) - Investigation. Sophie Cornu (SC) - Writing - Review & Editing, Conceptualization, Methodology, Formal analysis, Funding acquisition.

Declaration of competing interest

The authors declare that they have no known competing financial interests or personal relationships that could have appeared to influence the work reported in this paper.

Acknowledgements

The study is financially supported by project No KP-06-N34/2 funded by the Bulgarian National Science Fund and an internal CEREGE call. The authors are very thankful to Stoyan Vitanov - Geologist at Kaolinovo quarry for his enthusiastic and continuous logistic support during the field works. Magnetic hysteresis measurements were carried out at the Paleomagnetic laboratory in Bucharest with the generous hospitality of Prof. Dr. Cristian Panaiotu.

Appendix A. Supplementary data

Supplementary data to this article can be found online at <https://doi.org/10.1016/j.quascirev.2022.107671>.

References

- Antoine, P., Lagroix, F., Jordanova, D., Jordanova, N., Lomax, J., Fuchs, M., Debret, M., Rousseau, D.-D., Hatté, C., Gauthier, C., Moine, O., Taylor, S.N., Till, J.L., Coutard, S., 2019. A remarkable late saalian (MIS 6) loess (dust) accumulation in the lower Danube at Harletz (Bulgaria). *Quat. Sci. Rev.* 207, 80–100.
- Balescu, S., Lamothe, M., Mercier, N., Huot, S., Balteanu, D., Billard, A., Hus, J., 2003. Luminescence chronology of Pleistocene loess deposits from Romania: testing methods of age correction for anomalous fading in alkali feldspars. *Quat. Sci. Rev.* 22, 967–973.
- Balescu, S., Lamothe, M., Panaiotu, C., Panaiotu, C., 2010. La chronologie IRSL des séquences loessiques de l'est de la Roumanie. *Quaternaire* 115–126.
- Balescu, S., Jordanova, D., Brisson, L.F., Hardy, F., Huot, S., Lamothe, M., 2020. Luminescence chronology of the northeastern Bulgarian loess-paleosol sequences (Viatovo and Kaolinovo). *Quat. Int.* 552, 15–24.
- Buggle, B., Glaser, B., Zoller, L., Hambach, U., Markovic, S., Glaser, I., Gerasimenko, N., 2008. Geochemical characterization and origin of Southeastern and Eastern European loesses (Serbia, Romania, Ukraine). *Quat. Sci. Rev.* 27, 1058–1075.
- Buggle, B., Hambach, U., Müller, K., Zöller, L., Marković, S.B., Glaser, B., 2014. Iron mineralogical proxies and Quaternary climate change in SE-European loess-paleosol sequences. *Catena* 117, 4–22.
- Columbu, A., Spotl, C., De Waele, J., Yu, T.L., Shen, C.C., Gazquez, F., 2019. A long record of MIS 7 and MIS 5 climate and environment from a western Mediterranean speleothem (SW Sardinia, Italy). *Quat. Sci. Rev.* 220, 230–243.
- Cornell, R., Schwertmann, U., 2003. *The Iron Oxides. Structure, Properties, Reactions, Occurrence and Uses*. Weinheim, New York.
- Cravero, F., Churchman, J.G., 2016. The origin of spheroidal halloysites: a review of the literature. *Clay Miner.* 51, 417–427.
- Dearing, J.A., Hay, K.L., Baban, S.M.J., Huddleston, A.S., Wellington, E.M.H., Loveland, P.J., 1996. Magnetic susceptibility of soil: an evaluation of conflicting theories using a national data set. *Geophys. J. Int.* 127, 728–734.
- Dunlop, D., Ozdemir, O., 1997. In: Edwards, D. (Ed.), *Rock Magnetism. Fundamentals and Frontiers*, Cambridge Studies in Magnetism. Cambridge University Press.
- Evans, M., Heller, F., 2003. *Environmental Magnetism: Principles and Applications of Environmental Magnetism*. Academic Press, San Diego, CA.
- Evlogiev, Y., 2007. Evidence for the aeolian origin of loess in the danubian plain. *Geol. Balk.* 36 (3–4), 31–39.
- Eyre, J.K., 1996. The application of high resolution IRM acquisition to the discrimination of remanence carriers in Chinese loess. *Studia Geophys. Geod.* 40, 234–242.
- Fitzsimmons, K.E., Markovic, S.B., Hambach, U., 2012. Pleistocene environmental dynamics recorded in the loess of the middle and lower Danube basin. *Quat. Sci. Rev.* 41, 104–118.
- Francke, A., Wagner, B., Just, J., Leicher, N., Gromig, R., Baumgarten, H., Vogel, H., Lacey, J.H., Sadori, L., Wonik, T., Leng, M.J., Zanchetta, G., Sulpizio, R., Giaccio, B., 2016. Sedimentological processes and environmental variability at Lake Ohrid (Macedonia, Albania) between 637 ka and the present. *Biogeosciences* 13, 1179–1196.
- He, K., Zhao, X., Pan, Y., Zhao, X., Qin, H., Zhang, T., 2020. Benchmarking component analysis of remanent magnetization curves with a synthetic mixture series:

- insight into the reliability of unmixing natural samples. *J. Geophys. Res. Solid Earth* 125 (10), e2020JB020105.
- Heslop, D., 2015. Numerical strategies for magnetic mineral unmixing. In: *Earth-Science Reviews*, vol. 150, pp. 256–284.
- Hoyle, T.M., Bista, D., Flecker, R., Krijgsman, W., Sangiorgi, F., 2021. Climate-driven connectivity changes of the Black Sea since 430 ka: testing a dual palynological and geochemical approach. *Palaeogeogr. Palaeoclimatol. Palaeoecol.* 561, 110069.
- Hughes, P.D., Gibbard, P.L., Ehlers, J., 2019. The “missing glaciations” of the Middle Pleistocene. *Quat. Res.* 1, 23.
- IUSS Working Group WRB, 2015. World Reference Base for Soil Resources 2014, Update 2015 International Soil Classification System for Naming Soils and Creating Legends for Soil Maps. FAO, Rome. World Soil Resources Reports No. 106.
- Jia, X.X., Wu, H.M., Shao, M.A., Huang, L.M., Wei, X.R., Wang, Y.Q., Zhu, Y.J., 2020. Re-evaluation of organic carbon pool from land surface down to bedrock on China's Loess Plateau. *Agric. Ecosyst. Environ.* 293, 106842.
- Jipa, D.C., 2014. The conceptual sedimentary model of the Lower Danube loess basin: sedimentogenetic implications. *Quat. Int.* 351, 14–24.
- Jordanova, D., Hus, J., Evlogiev, J., Geeraerts, R., 2008. Palaeomagnetism of the loess/palaeosol sequence in Viatovo (NE Bulgaria) in the Danube basin. *Phys. Earth Planet. In.* 167, 71–83.
- Jordanova, D., Laag, C., Jordanova, N., Lagroix, F., Georgieva, B., Ishlyanski, D., Guyodo, Y., 2022. A detailed magnetic record of Pleistocene climate and distal ash dispersal during the last 800 kys - the Suhia Kladenetz quarry loess-palaeosol sequence near Pleven (Bulgaria). *Global Planet. Change* 214, 103840.
- Joussein, E., Petit, S., Churchman, J., Theng, B., Righi, D., Delvaux, B., 2005. Halloysite clay minerals - a review. *Clay Miner.* 40, 383–426.
- Koynov, V., Kabakchiev, I., Boneva, K., 1998. In: Koynov, V., Boneva, K. (Eds.), *Atlas of Soils in Bulgaria*. Zemizdat, Sofia.
- Lehmkuhl, F., Nett, J.J., Potter, S., Schulte, P., Sprafke, T., Jary, Z., Antoine, P., Wacha, L., Wolf, D., Zerboni, A., Hosek, J., Markovic, S.B., Obrecht, I., Sümege, P., Veres, D., Zeeden, C., Boemke, B., Schaubert, V., Viehweger, J., Hambach, U., 2021. Loess landscapes of Europe – mapping, geomorphology, and zonal differentiation. *Earth Sci. Rev.* 215, 103496.
- Leicher, N., Giaccio, B., Zanchetta, G., Wagner, B., Francke, A., Palladino, D.M., Sulpizio, R., Albert, P.G., Tomlinson, E.L., 2019. Central Mediterranean explosive volcanism and tephrochronology during the last 630 ka based on the sediment record from Lake Ohrid. *Quat. Sci. Rev.* 226, 106021.
- Lewis, D.G., Schwertmann, U., 1979. The influence of Aluminum on the formation of Iron Oxides. IV. The influence of Al, OH, and temperature. *Clay Clay Miner.* 27 (3), 195–200.
- Lisiecki, L.E., Raymo, M.E., 2005. A Pliocene-Pleistocene stack of 57 globally distributed benthic $\delta^{18}O$ records. *Paleoceanography* 20, PA1003. <https://doi.org/10.1029/2004PA001071>.
- Liu, Q., Roberts, A., Larrasoana, J., Banerjee, S., Guyodo, Y., Tauxe, L., Oldfield, F., 2012. Environmental magnetism: principles and applications. *Rev. Geophys.* 50, RG4002.
- Maher, B.A., 2011. The magnetic properties of Quaternary aeolian dusts and sediments, and their palaeoclimatic significance. *Aeol. Res.* 3, 87–144.
- Maher, B.A., 2016. Palaeoclimatic records of the loess/palaeosol sequences of the Chinese Loess Plateau. *Quat. Sci. Rev.* 154, 23–84.
- Margari, V., Skinner, L.C., Tzedakis, P.C., Ganopolski, A., Vautravers, M., Shackleton, N.J., 2010. The nature of millennial-scale climate variability during the past two glacial periods. *Nat. Geosci.* 3, 127–131.
- Marković, S.B., Hambach, U., Catto, N., Jovanović, M., Buggle, B., Machalet, B., Zöllner, G., Glaser, B., Frechen, M., 2009. The middle and late Pleistocene loess–palaeosol sequences at Batajanica, Vojvodina, Serbia. *Quat. Int.* 198, 255–266.
- Marković, S.B., Stevens, T., Kukla, G., Hambach, U., Fitzsimmons, K., Gibbard, P., Buggle, B., Zech, M., Guo, Z., Hao, Q., Wu, H., O'Hara Dhand, K., Smalley, I., Újvári, G., Sümege, P., Timar-Gabor, A., Veres, D., Sirocko, F., Vasiljević, D.A., Jary, Z., Svensson, A., Jović, V., Lehmkuhl, F., Kovács, J., Svirčev, Z., 2015. Danube loess stratigraphy — towards a pan-European loess stratigraphic model. *Earth Sci. Rev.* 148, 228–258.
- Maxbauer, D.P., Feinberg, J.M., Fox, D.L., 2016. MAX UnMix: a web application for unmixing magnetic coercivity distributions. *Comput. Geosci.* 95, 140–145.
- Mehra, O.P., Jackson, M.L., 1960. Iron oxide removal from soils and clays by a dithionite-citrate system buffered with sodium bicarbonate. *Clay Clay Miner.* 7, 317–327.
- Muhs, D.R., 2013. The geologic records of dust in the Quaternary. *Aeolian Res.* 9, 3–48.
- Necula, C., Dimofte, D., Panaiotu, C., 2015. Rock magnetism of a loess-palaeosol sequence from the western Black Sea shore (Romania). *Geophys. J. Int.* 202 (3), 1733–1748.
- Obrecht, I., Zeeden, C., Hambach, U., Veres, D., Markovic, S., Lehmkuhl, F., 2019. A critical reevaluation of palaeoclimate proxy records from loess in the Carpathian Basin. *Earth Sci. Rev.* 190, 498–520. <https://doi.org/10.1016/j.earscirev.2019.01.020>.
- Panaiotu, C.G., Panaiotu, E.C., Grama, A., Necula, C., 2001. Paleoclimatic record from a loess-paleosol profile in southeastern Romania. *Phys. Chem. Earth Solid Earth Geodes.* 26, 893–898. [https://doi.org/10.1016/S1464-1895\(01\)00138-7](https://doi.org/10.1016/S1464-1895(01)00138-7).
- Past Interglacials Working Group of PAGES, 2016. Interglacials of the last 800,000 years. *Rev. Geophys.* 54, 162–219. <https://doi.org/10.1002/2015RG000482>.
- Peel, M.C., Finlayson, B.L., McMahon, T.A., 2007. Updated world map of the Köppen-Geiger climate classification. *Hydrol. Earth Syst. Sci.* 11, 1633–1644.
- Pye, K., 1995. The nature, origin and accumulation of loess. *Quat. Sci. Rev.* 14, 653–667.
- Quantin, P., Gautheyrou, J., Lorenzoni, P., 1988. Halloysite formation through in situ weathering of volcanic glass from trachytic tuff, Vico's Volcano, Italy. *Clay Miner.* 23, 423–437.
- Radan, S.C., 2012. Towards a synopsis of dating the loess from the Romanian plain and Dobrogea: authors and methods through time. *Geo-Eco-Marina* 18, 153–172.
- Retallack, J., 2019. Alteration of paleosols after burial. In: *Soils of the Past: an Introduction to Paleopedology*, third ed. Wiley-Blackwell, ISBN 978-1-119-53045-9.
- Roberts, A.P., Tauxe, L., Heslop, D., Zhao, X., Jiang, Z., 2018. A critical appraisal of the “Day” diagram. *J. Geophys. Res. Solid Earth* 123, 2618–2644.
- Roberts, A.P., Hu, P., Harrison, R.J., Heslop, D., Muxworthy, A.R., Oda, H., et al., 2019. Domain state diagnosis in rock magnetism: evaluation of potential alternatives to the Day diagram. *J. Geophys. Res. Solid Earth* 124, 5286–5314.
- Robinson, S.G., 1986. The late pleistocene palaeoclimatic record of North Atlantic deep-sea sediments revealed by mineral-magnetic measurements. *Phys. Earth Planet. In.* 42, 22–47.
- Roucoux, K.H., Tzedakis, P.C., Lawson, I.T., Margari, V., 2011. Vegetation history of the penultimate glacial period (Marine isotope stage 6) at Ioannina, north-west Greece. *J. Quat. Sci.* 26, 616–626.
- Rousseau, D.-D., Antoine, P., Hatté, C., Lang, A., Zöllner, L., Fontugne, M., Ben Othman, D., Luck, J.-M., Moine, O., Labonne, M., Bentaleb, I., Jolly, D., 2002. Abrupt millennial climatic changes from Nussloch (Germany) upper Weichselian eolian records during the last glaciation. *Quat. Sci. Rev.* 21, 1577–1582.
- Sadori, L., Koutsodendris, A., Panagiotopoulos, K., Masi, A., Bertini, A., Combourieu-Nebout, N., Francke, A., Kouli, K., Joannin, S., Mercuri, A.M., Peyron, O., Torri, P., Wagner, B., Zanchetta, G., Sinopoli, G., Donders, T.H., 2016. Pollen-based paleoenvironmental and paleoclimatic change at Lake Ohrid (south-eastern Europe) during the past 500 ka. *Biogeosciences* 13, 1423–1437.
- Schirmer, W., 2016. Late pleistocene loess of the lower Rhine. *Quat. Int.* 411, 44–61.
- Schwertmann, U., Fitzpatrick, R.W., Taylor, R.M., Lewis, D.G., 1979. The influence of aluminum on iron oxides. Part II. Preparation and properties of Al-substituted hematites. *Clay Clay Miner.* 27, 105–112.
- Sheldon, N.D., Tabor, N.J., 2009. Quantitative paleoenvironmental and paleoclimatic reconstruction using paleosols. *Earth Sci. Rev.* 95, 1–52.
- Sierra, C.A., Hoyt, A.M., He, Y., Trumbore, S.E., 2018. Soil organic matter persistence as a stochastic process: age and transit time distributions of carbon in soils. *Global Biogeochem. Cycles* 32 (10), 1574–1588.
- Song, Y., Guo, Z., Marković, S.B., Hambach, U., Deng, C., Chang, L., Wu, J., Hao, Q., 2018. Magnetic stratigraphy of the Danube loess: a composite Titel-Stari Slankamen loess section over the last one million years in Vojvodina, Serbia. *J. Asian Earth Sci.* 155, 68–80.
- Spassov, S., Heller, F., Evans, M.E., Yue, L.P., Dobeneck, T.v., 2003. A lock-in model for the complex Matuyama–Brunhes boundary record of the loess/palaeosol sequence at Lingtai (Central Chinese Loess Plateau). *Geophys. J. Int.* 155, 350–366.
- Stephens, M., Krzyszkowski, D., Ivchenko, A., Majewski, M., 2003. Palaeoclimate and pedosedimentary reconstruction of a Middle to Late Pleistocene loess–palaeosol sequence. Pymorske, SW Ukraine. *Stud. Quat.* 19, 3–17.
- Sümege, P., Gulyás, S., Molnár, D., Sümege, B.P., Töröcsik, T., Imond, P.C., Smalley, I., Zhou, L., Galovic, L., Pál-Molnár, E., Hao, Q., Molnár, M., Koloszar, L., 2020. Periodicities of paleoclimate variations in the first high-resolution non-orbitally tuned grain size record of the past 1 Ma from SW Hungary and regional, global correlations. *Aeolian Res.* 40, 74–90.
- Tamm, O., 1922. Eine Method zur Bestimmung der anorganischen Komponenten des Golkomplex in Boden. *Meddelanden Statens Skogsförsöksanstalt* 19, 385–404.
- Thompson, R., Oldfield, F., 1986. *Environmental Magnetism*. Springer Science+Business Media B.V., Springer, Dordrecht.
- Tsai, C.C., Chen, Z.S., Kao, C.I., Ottner, F., Kao, S.J., Zehetner, F., 2010. Pedogenic development of volcanic ash soils along a climosequence in Northern Taiwan. *Geoderma* 156, 48–59.
- Vakhrameeva, P., Koutsodendris, A., Wulf, S., Fletcher, W.J., Appelt, O., Knipping, M., Gertisser, R., Trieloff, M., Pross, J., 2018. The cryptotephra record of the Marine Isotope Stage 12 to 10 interval (460–335 ka) at Tenaghi Philippon, Greece: exploring chronological markers for the Middle Pleistocene of the Mediterranean region. *Quat. Sci. Rev.* 200, 313–333.
- Vakhrameeva, P., Wulf, S., Koutsodendris, A., Tjallingii, R., Fletcher, W.J., Appelt, O., Ludwig, T., Knipping, M., Trieloff, M., Pross, J., 2019. Eastern Mediterranean volcanism during marine isotope stages 9 to 7e (335–235 ka): insights based on cryptotephra layers at Tenaghi Philippon, Greece. *J. Volcanol. Geoth. Res.* 380, 31–47.
- Vassilev, K., Apostolova, I., 2013. Bulgarian steppe vegetation: an overview. In: *Baumbach, H., Pfüzenreuter, S. (Eds.), Steppenlebensräume Europas: Gefährdung, Erhaltungsmaßnahmen und Schutz*. Thüringer Ministerium für Landwirtschaft, Forsten, Umwelt und Naturschutz, Erfurt, pp. 191–200.
- Wegwerth, A., Kaiser, J., Dellwig, O., Shumilovskikh, L.S., Nowaczyk, N.R., Arz, H.W., 2016. Northern hemisphere climate control on the environmental dynamics in the glacial Black Sea “Lake”. *Quat. Sci. Rev.* 135, 41–53.

- Wilson, G.P., Frogley, M.R., Hughes, P.D., Roucoux, K.H., Margari, V., Jones, T.D., Leng, M.J., Tzedakis, P.C., 2021. Persistent millennial-scale climate variability in southern Europe during marine isotope stage 6. *Quat. Sci. Adv.* 3, 100016.
- Wulf, S., Hardiman, M.J., Staff, R.A., Koutsodendris, A., Appelt, O., Blockley, S.P., Lowe, J.J., Manning, J., Ottoloni, L., Schmitt, A.K., Smith, V.C., Tomlinson, E.L., Vakhrameeva, P., Knipping, M., Kotthoff, U., Milner, A.M., Christanis, K., Kalaitzidis, S., Tzedakis, P.C., Schmedl, G., Pross, J., 2018. The marine isotope stage 1 - 5 cryptotephra record of Tenaghi Philippon, Greece: towards a detailed tepthrostratigraphic framework for the Eastern Mediterranean region. *Quat. Sci. Rev.* 186, 236–262.
- Zeeden, C., Hambach, U., Obrecht, I., Hao, Q., Abels, H.A., Veres, D., Frank Lehmkuhl, F., Milivoj, B., Gavrilov, M.B., Marković, S.B., 2018. Patterns and timing of loess-paleosol transitions in Eurasia: constraints for paleoclimate studies. *Global Planet. Change* 162, 1–7.